Dependence of CO_2 Breakthrough on the Sorbent Packing

Alexandra Gonchar[1], Vadim Lisitsa[2(✉)], Tatyana Khachkova[2], Dmitry Prokhorov[3], and Vladimir Derevschikov[3]

[1] Novosibirsk State University, Pirogova Street 2, 630090 Novosibirsk, Russia
[2] Institute of Petroleum Geology and Geophysics SB RAS, Koptug Avenue 3, 630090 Novosibirsk, Russia
lisitsavv@ipgg.sbras.ru
[3] Institute of Mathematics SB RAS, Koptug Avenue 4, 630090 Novosibirsk, Russia

Abstract. In this paper, we present a numerical study of the effect of the bulk sorbent particle packing on the break-through time. In our experiments, we fix the physical and chemical properties of the sorbent particles but vary the packing density (macroporosity) and the CO_2 volume fraction at the inlet. After that, the gas flow through the reactor is simulated, and CO_2 volume fraction as a function of time at the outlet is measured. We show that, in the case of high macroporosity, the recorded CO_2 concentration strongly depends on the macroporosity. On the contrary, if the macroporosity is low, we observe almost no difference in the break-through curves for the models with macroporosity less than 45%.

Keywords: Chemosorption · reactive transport · finite differences

1 Introduction

Carbon dioxide chemosorption is an important technology with several applications, such as fire safety and mine rescue equipment, inhalation anesthesia, respiratory care and others. The CO_2 sorbers are commonly based on the soda-lime porous sorbents, which supply the following chemical reaction $Ca(OH)_2 + CO_2 \rightarrow CaCO_3 \downarrow + H_2O$. Soda-lime sorbents are solid porous particles that are packed inside a reactor. The bulk sorbents' efficiency depends on the sorbent particles' physical and chemical properties, such as porosity, formation factor, efficient diffusion, chemical reaction rate, initial $Ca(OH)_2$ concentration, and others. However, bulk sorbents may have different packing densities, affecting the gas flow and advective transport of CO_2 in the inter-particle space.

In our previous research [10], we presented the numerical algorithm for direct computational fluid dynamics simulation of gas flow in the reactor filled with the bulk sorbent and further CO_2 transport and chemosorption by the sorbent particles. We paid primary attention to the properties of the sorbent, i.e.,

The research was supported by the Russian Science Foundation grant no. 21–71-20003.

© The Author(s), under exclusive license to Springer Nature Switzerland AG 2024
O. Gervasi et al. (Eds.): ICCSA 2024 Workshops, LNCS 14817, pp. 290–304, 2024.
https://doi.org/10.1007/978-3-031-65238-7_20

porosity, effective diffusion, and reaction rate. In particular, we simulated CO_2 sorption by a single particle and investigated the chemical compound of the particle at different time instants. Numerical simulations were compared over the lab measurements, which let us calibrate the mathematical model. In particular, we estimated the formation factor and chemical reaction rates for Loflosorb particles [2].

However, particle packing density may also affect the efficiency of CO_2 sorption due to differences in the inter-particle space geometry, which may affect the CO_2 transport. This paper presents a numerical study of the packing density on the break-through curves (dependence on CO_2 concentration at the outlet on time). We generated several statistical realizations of spherical particle packing for four different packing densities (macro-porosity values). After that, we simulated the advection-diffusion reaction process inside the reactor and recorded CO_2 concentration at the outlet to investigate how strong the relation between the bulk sorbent packing density and the efficiency of CO_2 sorption.

2 Mathematical Problem Formulation

We assume the model has two types of pores. The reciprocal positions of the sorbent particles form the macropores. This type of pore space is the main objective of current research. Macropores support both the advection and the diffusion of CO_2. The second type of pores are the micropores inside the sorbent particles. The particular sorbent defines this pore space and can not be changed during the experiments. We assume that only the diffusion of CO_2 is allowed in micropores and no advection.

We introduce the domain D, where the chemosorption process is considered. This domain is a union of two non-overlapping subdomains D_p and D_g, which are the macro- and microporous spaces, respectively. Sketches of the computational domains for two different sorbent packs are presented in Fig. 1.

We assume that the fluid flow is allowed inside the macropores D_p. To simplify further considerations, the fluid is assumed to be incompressible; moreover, the chemosorption process is slow, with no changes in model geometry. Thus, we may deal with the steady-state flow satisfying the steady-state Stokes equation in D_p:

$$\nabla p - \mu \Delta \vec{u} = 0, \nabla \cdot \vec{u} = 0. \tag{1}$$

On the contrary, no flow is allowed in the micropores D_g, thus

$$\vec{u} = 0. \tag{2}$$

In this notation, $p(\vec{x})$ is the fluid pressure, $\vec{u}(\vec{x})$ is the fluid flow velocity, and μ is the dynamic viscosity of the fluid.

We need to state the boundary conditions to resolve the fluid flow inside the macropores. Let us consider several types of boundaries. First, the interfaces between the macroporous space, the sorbent particles, and the sides of the reactor (Fig. 2). We pose the no flow conditions at these interfaces Γ:

$$\vec{u} = 0. \tag{3}$$

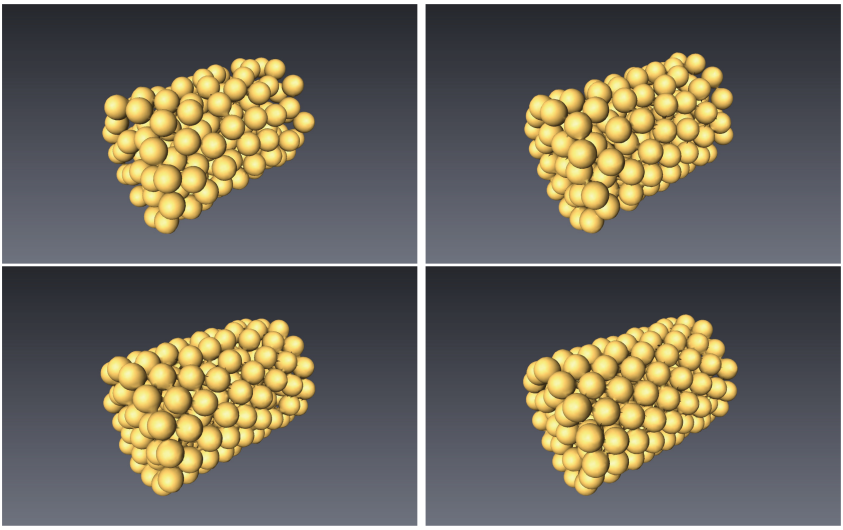

Fig. 1. Sketches of the computational domains. The Interior of the spherical particles corresponds to the microporous space D_g, and the exterior corresponds to D_p. The porosity of the left top model is 55%, porosity of the right top model is 50%, porosity of the left bottom model is 45%, and porosity of the right bottom model is 40%.

Second boundary type is the inlet Γ_{in} defied as $x_1 = x_1^{in}$, where flow rate is defined according to the formula:

$$Q(x_1^{in}) = \int_{x_2,x_3} v_1(x_1^{in}, x_2, x_3) dx_2 dx_3 = Q_{in}. \tag{4}$$

Third boundary type is the outlet Γ_{out} defied as $x_1 = x_1^{out}$, where the pressure is fixed:

$$p(x_1^{out}) = p^{out}. \tag{5}$$

The equation governing the reactive transport can be stated inside the entire computational domain $D = D_g \cup D_p$:

$$\frac{\partial}{\partial t}(\phi C_j) + \nabla \cdot (\vec{u} C_j) - \nabla \cdot (D_j \nabla C_j) = g_j(\vec{C}). \tag{6}$$

In these notations, C_j represents the molar concentration of chemical species, D_j is the diffusion coefficient of the particular species, ϕ is the open porosity of the microporous material, functions $g_j(\vec{C})$ are defined by the chemical reactions. It is clear that for the macropores, porosity equals one ($\phi = 1$) and $\vec{u}(\vec{x})$ is the flow velocity which is the solution of Stokes equation (1), and the diffusion coefficients D_j correspond to molecular diffusion of the particular species; i.e., $D_j = D_j^0$. On the contrary, in the microporous space, the porosity is less than one ($\phi < 1$), the flow rate is zero ($\vec{u} = 0$), and the diffusion coefficient is reduced

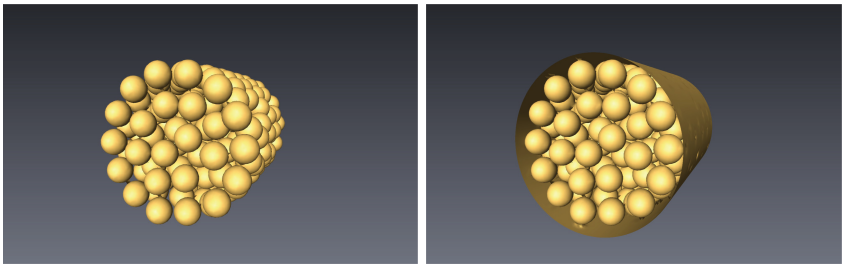

Fig. 2. Sketches of the computational domains without the reactor sides (left) and with the reactor (right).

according to the estimate $D_j = \phi D_j^0 / F$, where F is the formation factor [6]. For most porous materials, the formation factor is bounded as $F \in [1, 10]$.

In this paper, we simulate the CO_2 chemosorption by the soda-lime sorbent, which satisfy the following reaction equation:

$$Ca(OH)_2 + CO_2 \rightarrow CaCO_3 + H_2O. \tag{7}$$

Among these species, CO_2 and H_2O are movable. Thus, their transport satisfies the advection-diffusion-reaction equation (6), whereas $Ca(OH)_2$ and $CaCO_3$ are immovable, their concentrations change only due to the chemical reaction.

The advection-diffusion-reaction system requires the initial conditions for all species and boundary conditions for movable species. The initial conditions are

$$\begin{aligned} &C_j(\vec{x}, 0) = 0, \quad \vec{x} \in D_p,\ i = 1, ..., J; \\ &C_m(\vec{x}, 0) = 0, \quad \vec{x} \in D_g,\ m = 1, ..., M; \\ &C_i(\vec{x}, 0) = C_i^0,\ \vec{x} \in D_g,\ i = M+1, ..., J \end{aligned}$$

where, following [10], C_j corresponds to all considered species, C_m, $m = 1, ..., M$ represents the movable species, and C_i, $i = m+1, ..., J$ corresponds to immovable species. The presented initial conditions set concentrations of all species to zero in the macropores. Movable species are not present in the microporous space either. On the contrary, immovable species are defined as nontrivial inside the sorbent particles.

We also need to state the boundary conditions for the movable species. They are

$$\begin{aligned} &C_m(x_1^{in}, t) = C_m^{in},\ \vec{x} \in x_1^{in} \quad m = 1, ..., M; \\ &\tfrac{\partial C_m}{\partial \vec{n}}(\vec{x}, t) = 0, \qquad \vec{x} \in x_1^{out}\ m = 1, ..., M. \\ &\tfrac{\partial C_m}{\partial \vec{n}}(\vec{x}, t) = 0, \qquad \vec{x} \in \Gamma_{ext}\ m = 1, ..., M. \end{aligned}$$

The first set of conditions defines the concentrations of movable species at the inlet. The second set of conditions is defined at the outlet, stating the free flow condition. The last set of equations is stated at the sides of the reactor, and they guarantee that no external factors affect the concentrations at this surface. Note that the advection-diffusion-reaction equations are stated inside the entire

computational domain; thus, no explicit conditions are required at the interface between the macropores and sorbent particles.

We also need to specify the reactive part of the Eq. (6). Chemosorption of CO_2 by soda-lime sorbent satisfy the reaction (7) with the following kinetics:

$$\begin{array}{c} \frac{\partial}{\partial t}\left(\phi C_{CO_2}\right) + \nabla \cdot \left(\vec{u} C_{CO_2}\right) - \nabla \cdot \left(D_{CO_2} \nabla C_{CO_2}\right) = -k\phi C_{CO_2} C_{Ca(OH)_2}, \\ \frac{\partial}{\partial t}\left(\phi C_{H_2O}\right) + \nabla \cdot \left(\vec{u} C_{H_2O}\right) - \nabla \cdot \left(D_{H_2O} \nabla C_{H_2O}\right) = k\phi C_{CO_2} C_{Ca(OH)_2}, \\ \frac{\partial}{\partial t}\left(C_{Ca(OH)_2}\right) = -k\phi C_{CO_2} C_{Ca(OH)_2}, \\ \frac{\partial}{\partial t}\left(C_{CaCO_3}\right) = k\phi C_{CO_2} C_{Ca(OH)_2}, \end{array} \tag{8}$$

Note that the considered reactions are irreversible, and the concentration of the species products does not depend on the concentration of the products, i.e., C_{H_2O} and C_{CaCO_3}. Moreover, transport of CO_2 does not depend on water or $CaCO_3$ concentration; thus, these two species may be excluded from the considerations. In our previous research [10], we computed the $CaCO_3$ concentration to compare the simulation results with the lab experiments. However, such data is unavailable for the break-through experiments.

The reduced system of advection-diffusion-reaction system can be represented as

$$\begin{array}{c} \frac{\partial}{\partial t}\left(\phi C_{CO_2}\right) + \nabla \cdot \left(\vec{u} C_{CO_2}\right) - \nabla \cdot \left(D_{CO_2} \nabla C_{CO_2}\right) = -k\phi C_{CO_2} C_{Ca(OH)_2}, \\ \frac{\partial}{\partial t}\left(C_{Ca(OH)_2}\right) = -k\phi C_{CO_2} C_{Ca(OH)_2}, \end{array} \tag{9}$$

with the following boundary and initial conditions:

$$\begin{array}{ll} C_{CO_2} = C^{in}_{CO_2}, & \vec{x} \in x^{in}_1 \\ \frac{\partial C_{CO_2}}{\partial \vec{n}} = 0, & \vec{x} \in x^{out}_1 \\ \frac{\partial C_{CO_2}}{\partial \vec{n}} = 0, & \vec{x} \in \Gamma_{ext} \end{array} \tag{10}$$

$$\begin{array}{ll} C_{CO_2}(0, \vec{x}) = 0, & \vec{x} \in D_p \cup D_g, \\ C_{Ca(OH)_2}(0, \vec{x}) = 0, & \vec{x} \in D_p, \\ C_{Ca(OH)_2}(0, \vec{x}) = C^0_{Ca(OH)_2}, & \vec{x} \in D_g, \end{array} \tag{11}$$

3 Numerical Methods

Numerical methods and implemented numerical algorithms to solve the considered problem in models with irregular interfaces are discussed in detail in [10]. Here, we briefly remind the main aspects.

In this research, we use finite differences on regular rectangular (cubic) grids to approximate the Stokes and advection-diffusion-reaction equations. Thus, we need to apply special techniques to account for the sorbent particles' spherical form and the reactor's cylindrical form. It can be efficiently done using the level-set method [4,9,14,16] in combination with the immersed boundaries method [5,8,9,13]. Moreover, two level-sets $\varphi^p(\vec{x})$ and $\varphi^e(\vec{x})$ are defined to distinguish the interfaces between the macroporous and microporous domains and between the interior and exterior of the reactor, respectively. The two interfaces are equivalent

for the fluid flow solver because they are impermeable to the fluid flow. However, the two types of interfaces are treated differently when the advection-diffusion-reaction equation is solved.

The approximation of Stokes equation is based on the second-order accurate finite differences on staggered grids. The pressure is defined in integer points, whereas the velocity components are stored at the points with one half-integer index; for example, u_1 is defined in points $((x_1)_{i+1/2}, (x_2)_j, (x_3)_k)$. Note that Stokes equation is approximated only in macropores, thus for $\varphi^p(\vec{x}) > 0$ and $\varphi^e(\vec{x}) > 0$. The projection-type methods are used to solve an obtained system of linear algebraic equations, where the Krylov-type methods treat the Poisson equation with spectral preconditioner [7].

Advection-diffusion-reaction equations are solved with the operator splitting technique. We apply the AD-R splitting scheme, where the prediction step is applied to solve the coupled advection-diffusion part of the equation, and then the correction is performed to account for the reaction. The advection term is approximated using the third-order WENO scheme [11,16,17], whereas the diffusion part is approximated with the second-order central differences [7].

Approximation of the reactive part is based on the implicit time stepping scheme, which is unconditionally stable, but the time step is used to preserve the desired accuracy level. The details of the approximation are provided in [10].

4 Model Construction

To generate the model of the reactor filled with the spherical sorbent particles with required porosity we used Lubachevsky-Stillinger algorithm [12] as in [1].

The Lubachevsky-Stillinger algorithm simulates motion and interaction of elastic spherical particles with increasing radius. At the beginning of the simulation the spheres have zero radii, random positions and velocities. The algorithm implements event-based approach. Therefore, it consists of two main parts: computation of interaction time and velocities recalculation. In case of particle-particle interaction both parts are described in [12] (2D) and [15] (3D). However, the usual domain for packing by Lubachevsky-Stillinger is a rectangle with periodic boundary, which differs from current case: cylinder with impenetrable boundary. Thus, in this section we describe our approach to particle-boundary interactions.

Let us assume a cylinder in $\mathbb{R}^3$ with radius R and height H, whose height coincides with Z-axis from 0 to H. The state of the particle is defined by seven parameters (x, y, z) — coordinate of the center, (v_x, v_y, v_z) — velocity vector, r — radius. The initial arrangement is chosen randomly:

$$\begin{aligned} x &= R\sqrt{r_u}\cos\phi, & v_x &= \sqrt{1-(2u-1)^2}\cos\theta, \\ y &= R\sqrt{r_u}\sin\phi, & v_y &= \sqrt{1-(2u-1)^2}\sin\theta, \\ z &= Hh_u, & v_z &= 2u-1, \\ r &= 0, \end{aligned}$$

where u, h_u, r_u are random variables with uniform distribution on the segment $[0, 1]$, ϕ and θ are random variables with uniform distribution on the segment $[0, 2\pi]$. The radius growth rate is assumed to be linear $r = at$.

The interaction time with the bottom base of the cylinder can be computed by the formula:

$$t_i = t_c + \frac{z - at_c}{a - v_z},$$

where t_c is the current time. Similarly, interaction time with the top base is:

$$t_i = t_c + \frac{H - z - at_c}{a + v_z}.$$

The interaction time with the side is t_c plus the minimal positive value of the equation:

$$\begin{aligned} &At^2 + 2Bt + C = 0, \\ &A = v_x^2 + v_y^2 - a^2, \\ &B = xv_x + yv_y + a(R - at_c), \\ &C = x^2 + y^2 - (R - at_x)^2. \end{aligned}$$

To avoid the intersection of the growing sphere with the boundary, we increase the velocity after the interaction, so in the case of cylinder bases, this leads to the following expression for velocities:

$$\begin{aligned} v_x^{new} &= v_x \\ v_y^{new} &= v_y \\ v_z^{new} &= \pm(|v_z| + 1.1a), \end{aligned}$$

where $+$ sign corresponds to bottom base, $-$ to top base. However, on a side with negative curvature, the velocity increase may be large if the angle of particle incidence is acute. High velocities cause small intervals between steps [12], so for simplicity, we reflect particles perpendicular to side:

$$\begin{aligned} v_x^{new} &= -\frac{x(\sqrt{v_x^2 + v_y^2} + 1.1a)}{\sqrt{x^2 + y^2}}, \\ v_y^{new} &= -\frac{y(\sqrt{v_x^2 + v_y^2} + 1.1a)}{\sqrt{x^2 + y^2}}, \\ v_z^{new} &= v_z. \end{aligned}$$

The algorithm takes as input H, R, r_s (radius of sorbent particles), ρ (dimensionless density), computes required number of particles $N = \frac{3\rho HR^2}{4r_s^3}$, creates random initial configuration and performs iterations until $r = r_s$.

5 Numerical Experiments

To perform the numerical experiments estimating the breakthrough time in dependence on the packing density, we considered a cylindrical reactor with a diameter of 17 mm and a length of 24 mm. It was filled with spherical sorbent particles 3 mm in diameter. We simulated the breakthrough process for the Soda-lime Loflosorb (Intersurgical Ltd, UK). This commercially available CO_2 sorbent is used in breathing systems to absorb exhaled carbon dioxide during anesthesia. Note that in the previous research [10], we calibrate the mathematical model to match this sorbent's formation factor and reaction rate. Loflosorb contains 60 wt% of $Ca(OH)_2$, 15 wt% of water, and less than 0.1 wt% of the indicator (ethyl violet) [3]. The mass density of the granules, porosity (measured in m^3/kg), and mass fraction of H_2O, $Ca(OH)_2$, and $CaCO_3$ at the initial stage were measured in a lab. They are provided in Table 1, as well as an estimation of the formation factor and the chemical reaction rate. In particular, we focused on the experiments with a fixed form factor equal to 5 and a reaction rate equal to 10^{-3}. The material's dimensionless porosity equals 0.49 as follows from computations, presented in [10]. Note that all provided parameters characterize the sorbent and can not be changed in a lab.

Table 1. Measured properties of the sorbent at the initial stage.

property	notation	Loflosorb
density (kg/m^3)	ρ	1080
chem. porosity (m^3/kg)	v_p	$4.6 \cdot 10^{-4}$
mass fraction of $Ca(OH)_2$	$\mu_{Ca(OH)_2}$	0.76
mass fraction of $CaCO_3$	μ_{CaCO_3}	0.05
Form factor	F	5–9
reaction rate	k	$10^{-3} - 10^{-2}$

On the contrary, the variable parameters in the breakthrough experiments are the density of the particle packing and CO_2 concentration at the inlet. To reduce the number of simulations, we focused only on the rapid flows corresponding to 15 liters per hour flow rates or $4.14 \cdot 10^{-6}$ m^3/s. We considered three values of CO_2 concentration at the inlet equal to 1, 5, and 7% of volumetric concentration. We also considered four different values of particle packing density characterized by the macroporosity (ratio of the volume of macropores to the volume of the entire reactor), which was 40, 45, 50, and 55 %. Note that the reactor diameter is about five diameters of the particles; achieving smaller porosity (denser packing) is impossible due to the side effects. Examples of different packing are provided in Fig. 1. We generated ten statistical realizations for each packing density to estimate the mean and STD of the concentrations at the outlet. Thus, a total of 120 simulations were done.

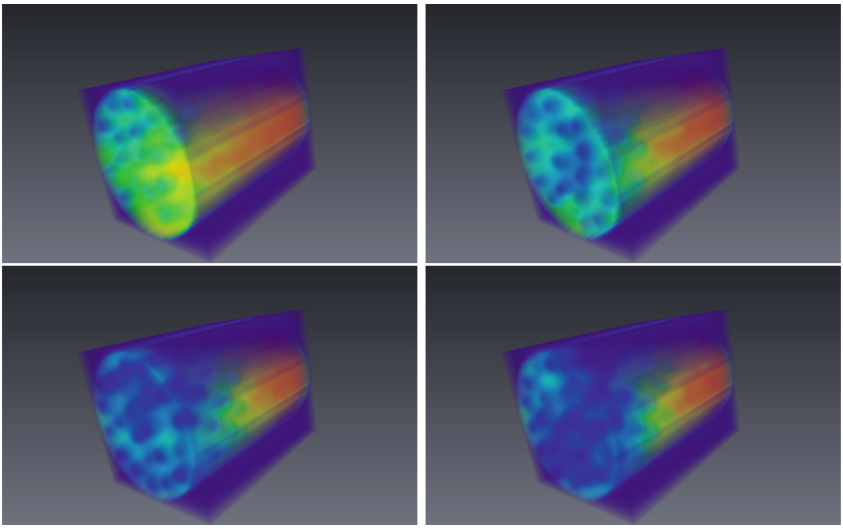

Fig. 3. The concentration of CO_2 in the computational domain at time instant $t = 7200$ s. Colorbar changes from blue ($C_{CO_2} = 0$) to red where $C_{CO_2} = 7\%$. The porosity of the left top model is 55%, porosity of the right top model is 50%, porosity of the right bottom model is 45%, and porosity of the right bottom model is 40%. (Color figure online)

First, we consider CO_2 concentration inside the reactor as presented in Fig. 3. Concentration gradually decreases from the inlet to the outlet of the reactor. It illustrates that the sorption acquires closer to the inlet, significantly preventing CO_2 penetration further to the outlet. However, as time passes, soda-lime concentration reduces near the inlet, opening the way for CO_2 flow closer to the outlet.

We also provide the 2D cross-sections of the concentration plots inside the reactor in Figs. 4, 5, 6. We considered the X_1X_2 cross-section where X_1 is the direction along the reactor, and X_2 is orthogonal to the reactor axis. We illustrate three cases corresponding to different CO_2 concentrations at the inlet, i.e., 7, 5, and 1 % of the volumetric fraction. In the cases of high values of macroporosity, the concentration field is inhomogeneous due to the existence of preferred fluid flow channels that support advective transport. On the contrary, if the macroporosity is low (45 and 40%), the reaction front is relatively homogeneous. Moreover, the propagation speed of the reaction front is approximately the same for the samples with low macroporosity. These effects are observable in Figs. 4 and 5 where the CO_2 concentration is high at the inlet. In the case of low CO_2 concentration at the inlet, the reaction front did not penetrate deep enough into the reactor because the particles close to the inlet can still do CO_2 sorption.

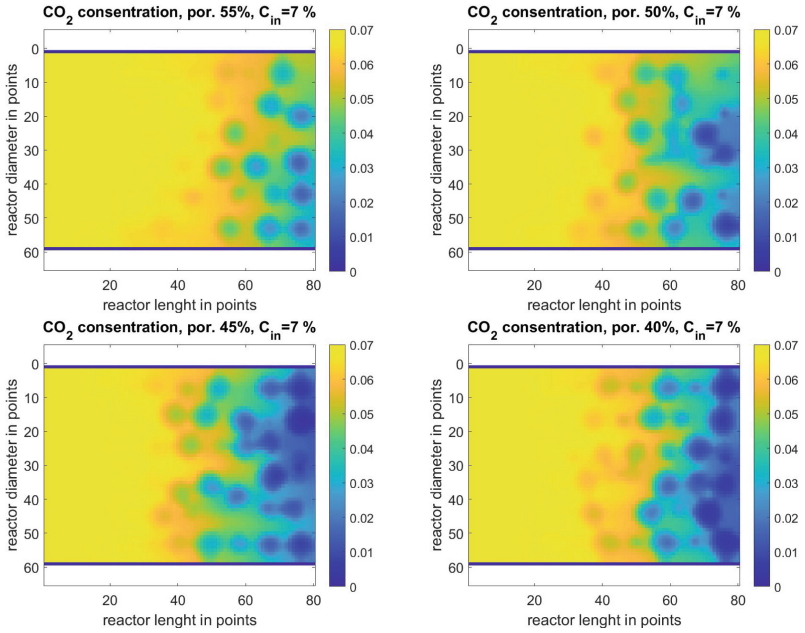

Fig. 4. The cross-section plots of CO_2 volume fraction inside the reactor at time instant $t = 7200$ s, CO_2 volume fraction at the inlet is 7%. The porosity of the left top model is 55%, porosity of the right top model is 50%, porosity of the right bottom model is 45%, and porosity of the right bottom model is 40%.

We also recorded CO_2 concentration at the outlet as a function of time. Time sampling was 7.2 s; the data was acquired at 1000 time instants. Figures 7, 8, 9 represent the break-through curves for different macroporosity values and CO_2 volume fraction at the inlet. As mentioned above, we performed simulations for ten different statistical realizations of the models with fixed macroporosity. Figures 7, 8, 9 provide the curves for all experiments. Note that in the case of high macroporosity (55 and 50%), the results for different realizations are close to each other (curves of the same color). It is due to the "homogeneity" of the flow in the macropore space. On the contrary, if the porosity is low, the fluid flow path becomes complex and may strongly depend on the pore space geometry, thus on the statistical realization of the model. Also, if the experiments with high macroporosity values are compared, one may note that the recorded

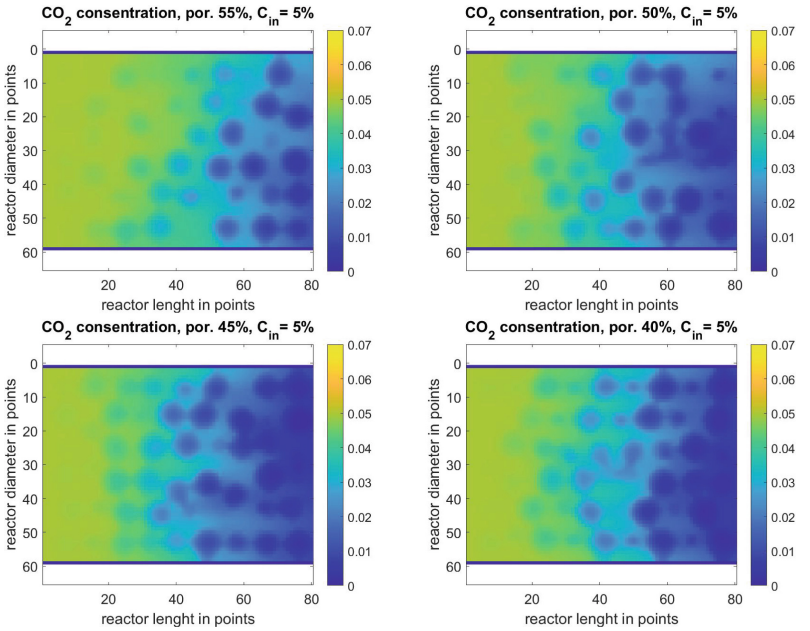

Fig. 5. The cross-section plots of CO_2 volume fraction inside the reactor at time instant $t = 7200$ s, CO_2 volume fraction at the inlet is 5%. The porosity of the left top model is 55%, porosity of the right top model is 50%, porosity of the right bottom model is 45%, and porosity of the right bottom model is 40%.

CO_2 concentration strongly depends on the macroporosity. In particular, for the experiments with 7% of CO_2 volume fraction at the inlet, the concentration at the outlet at $t = 7200$ s is about 2% for models with $\phi = 55\%$, is 1.5% for models with $\phi = 50\%$, and 1% for models with $\phi \geq 55\%$. On the contrary, we observe almost no difference in the break-through curves for the models with macroporosity greater than 55%.

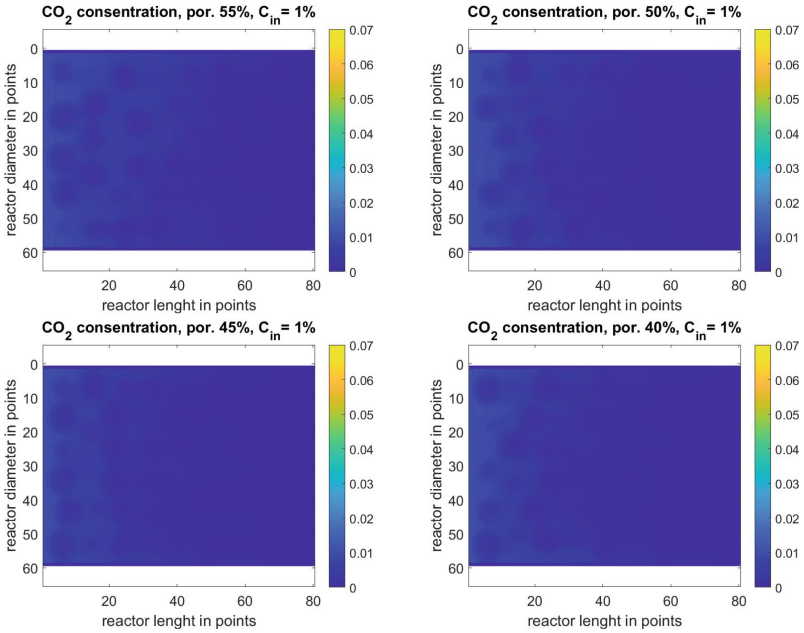

Fig. 6. The cross-section plots of CO_2 volume fraction inside the reactor at time instant $t = 7200$ s, CO_2 volume fraction at the inlet is 1%. The porosity of the left top model is 55%, porosity of the right top model is 50%, porosity of the right bottom model is 45%, and porosity of the right bottom model is 40%.

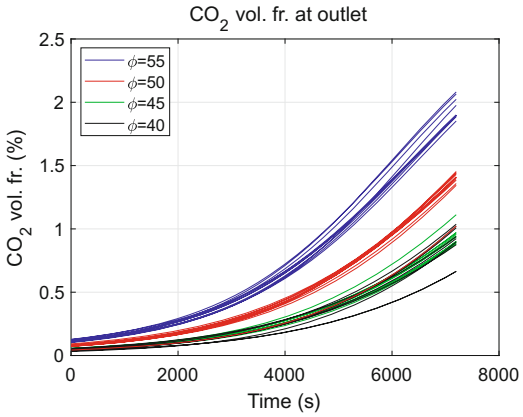

Fig. 7. The volume fraction of CO_2 at the outlet for different macroporosity inside the reactor. The volume fraction at the inlet is 7%.

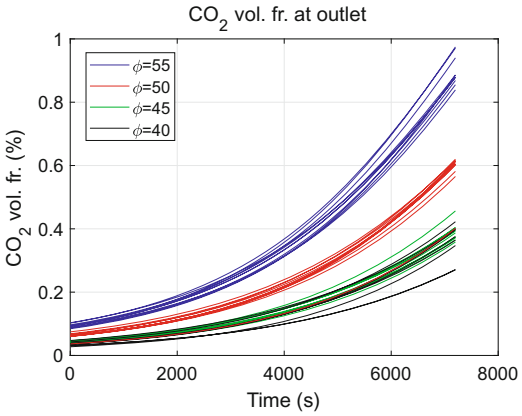

Fig. 8. The volume fraction of CO_2 at the outlet for different macroporosity inside the reactor. The volume fraction at the inlet is 5%.

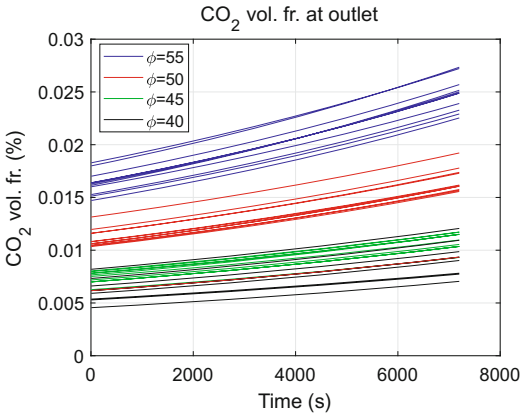

Fig. 9. The volume fraction of CO_2 at the outlet for different macroporosity inside the reactor. The volume fraction at the inlet is 1%.

6 Conclusion

In this paper, we presented the numerical algorithm to simulate the chemisorption of CO_2 by Soda-lime sorbent. The algorithm is based on a finite-difference approximation of the Stokes and advection-diffusion-reaction equation. We use the explicit finite differences for approximating the advection-diffusion term and the implicit approximation of the reaction term, solving the ADR equation with the splitting technique. The algorithm is implemented using CUDA technology; thus, it is oriented toward the use of GPUs.

We use the designed algorithm to study the effect of sorbent particle packing on the break-through time. In our experiments, we fixed the physical and chemical properties of the sorbent particles but varied the packing density

(macroporosity) and the CO_2 volume faction at the inlet. After that, the gas flow through the reactor was simulated for up to 7200 s of the model time. We measured the CO_2 volume fraction as a function of time at the outlet and fixed the volume fraction inside the reactor at the last instant.

We observed that, in the cases of high values of macroporosity, the CO_2 concentration field inside the reactor is inhomogeneous due to preferred fluid flow channels supporting advective transport. On the contrary, if the macroporosity is low (45 and 40%), the reaction front is relatively homogeneous. At the same time, if the break-through curves are considered, one may note that in the case of high macroporosity (55 and 50%), the results for different statistical realizations of the model are close to each other (curves of the same color). On the contrary, if the porosity is low, the fluid flow path becomes complex and may strongly depend on the pore space geometry, thus on the statistical realization of the model. Also, if the experiments with high macroporosity values are compared, one may note that the recorded CO_2 concentration strongly depends on the macroporosity. In particular, for the experiments with 7% of CO_2 volume fraction at the inlet, the concentration at the outlet at $t = 7200$ s is about 2% for models with $\phi = 55\%$, is 1.5% for models with $\phi = 50\%$, and 1% for models with $\phi \geq 55\%$. On the contrary, we observe almost no difference in the break-through curves for the models with macroporosity less than 45%.

References

1. Bazaikin, Y., Malkovich, E., Prokhorov, D., Derevschikov, V.: Detailed modeling of sorptive and textural properties of CaO-based sorbents with various porous structures. Sep. Purif. Technol. **255**, 117746 (2021). https://doi.org/10.1016/j.seppur.2020.117746
2. Derevschikov, V.S., Kazakova, E.D., Yatsenko, D.A., Veselovskaya, J.V.: Multiscale study of carbon dioxide chemisorption in the plug flow adsorber of the anesthesia machine. Sep. Sci. Technol. **56**(3), 485–497 (2021)
3. Derevshchikov, V.S., Kazakova, E.D.: Comparative analysis of the chemical composition and sorption, textural, and strength properties of commercial medical co2 sorbents. Catal. Ind. **12**(1), 1–6 (2020)
4. Gibou, F., Fedkiw, R., Osher, S.: A review of level-set methods and some recent applications. J. Comput. Phys. **353**, 82–109 (2018)
5. Johansen, H., Colella, P.: A cartesian grid embedded boundary method for Poisson's equation on irregular domains. J. Comput. Phys. **147**(1), 60–85 (1998)
6. Khachkova, T., Lisitsa, V., Kolyukhin, D., Reshetova, G.: Influence of interfaces roughness on elastic properties of layered media. Probab. Eng. Mech. **66**, 103170 (2021)
7. Khachkova, T., Lisitsa, V., Reshetova, G., Tcheverda, V.: GPU-based algorithm for evaluating the electrical resistivity of digital rocks. Comput. Math. Appl. **82**, 200–211 (2021)
8. Li, X., Huang, H., Meakin, P.: Level set simulation of coupled advection-diffusion and pore structure evolution due to mineral precipitation in porous media. Water Resour. Res. **44**(12), W12407 (2008)

9. Lisitsa, V., Bazaikin, Y., Khachkova, T.: Computational topology-based characterization of pore space changes due to chemical dissolution of rocks. Appl. Math. Model. **88**, 21–37 (2020). https://doi.org/10.1016/j.apm.2020.06.037
10. Lisitsa, V., Khachkova, T., Bazaikin, Y., Derevschikov, V.: Simulation of co_2 sorption from the gas stream by the grain of soda-lime sorbent. In: Gervasi, O., Murgante, B., Misra, S., Rocha, A.M.A.C., Garau, C. (eds.) Computational Science and Its Applications - ICCSA 2022 Workshops, pp. 334–347. Springer International Publishing (2022). https://doi.org/10.1007/978-3-031-10592-0_25
11. Liu, X.D., Osher, S., Chan, T.: Weighted essentially non-oscillatory schemes. J. Comput. Phys. **115**(1), 200–212 (1994)
12. Lubachevsky, B.D., Stillinger, F.H.: Geometric properties of random disk packings. J. Stat. Phys. **60**, 561–583 (1990)
13. Luo, K., Zhuang, Z., Fan, J., Haugen, N.E.L.: A ghost-cell immersed boundary method for simulations of heat transfer in compressible flows under different boundary conditions. Int. J. Heat Mass Transf. **92**, 708–717 (2016)
14. Osher, S., Fedkiw, R.P.: Level set methods: an overview and some recent results. J. Comput. Phys. **169**(2), 463–502 (2001)
15. Pollmann, N., Larsson, F., Runesson, K., Lundgren, K., Zandi, K., Jänicke, R.: Modeling and computational homogenization of chloride diffusion in three-phase meso-scale concrete. Constr. Build. Mater. **271**, 121558 (2021). https://doi.org/10.1016/j.conbuildmat.2020.121558
16. Prokhorov, D., Lisitsa, V., Khachkova, T., Bazaikin, Y., Yang, Y.: Topology-based characterization of chemically-induced pore space changes using reduction of 3d digital images. J. Comput. Sci. **58**, 101550 (2022)
17. Qiu, J.M., Shu, C.W.: Conservative high order semi-Lagrangian finite difference WENO methods for advection in incompressible flow. J. Comput. Phys. **230**(4), 863–889 (2011)